






Coherent acoustic phonon dynamics facilitating acoustic deformation potential characterization of Mg_3Sb_2

Pengbo Ding ^{1,*}, Yifan Zhu,^{2,*} Zhijia Han ^{3,*}, Long Li,^{1,4} Liang Zhang,^{1,5} Yuhang Cai,¹ David J. Singh ⁶, Lenan Zhang,⁷ Wenqing Zhang,³ Sunmi Shin ⁵, Jiong Yang,^{8,9,†} Weishu Liu,^{3,‡} and Liang Guo ^{1,§}

¹*Department of Mechanical and Energy Engineering, Southern University of Science and Technology, Shenzhen, China*

²*State Key Laboratory of High Performance Ceramics and Superfine Microstructure, Shanghai Institute of Ceramics, Chinese Academy of Sciences, Shanghai, China*

³*Department of Materials Science and Engineering, Southern University of Science and Technology, Shenzhen, China*

⁴*School of Microelectronics, Shenzhen Institute of Information Technology, Shenzhen, China*

⁵*Department of Mechanical Engineering, National University of Singapore, Singapore*

⁶*Department of Physics and Astronomy, University of Missouri, Columbia, Missouri 65211, USA*

⁷*Department of Mechanical Engineering, Massachusetts Institute of Technology, Cambridge, Massachusetts 02139, USA*

⁸*Materials Genome Institute, Shanghai University, Shanghai, China*

⁹*Zhejiang Laboratory, Hangzhou, Zhejiang, China*



(Received 4 July 2022; revised 6 August 2023; accepted 7 August 2023; published 21 August 2023)

Acoustic deformation potential (ADP) quantifies carrier-acoustic phonon coupling and is essential for dissecting transport physics in thermoelectrics. Herein, we report the use of ultrafast spectroscopy of coherent acoustic phonons (CAPs) to characterize the ADP of thermoelectric materials, using Mg_3Sb_2 as an example. The photon energy-dependent amplitudes of the CAP-induced oscillatory reflectance were used to determine the ADP coupling constant, agreeing well with that from first-principles calculations. This method relies on the transient Coulombic interaction between carriers and acoustic phonons, free of influence from other scattering channels. It is shown that the method is particularly feasible for the study of thermoelectric materials, because their common features of strong phonon anharmonicity and small band gaps make the measurement insensitive to the uncertainty of carrier diffusion coefficients, ensuring its accuracy.

DOI: [10.1103/PhysRevB.108.064310](https://doi.org/10.1103/PhysRevB.108.064310)

I. INTRODUCTION

The contrasting electrical and thermal transport requirements for high-performance thermoelectric materials drive the fundamental studies on carrier and phonon dynamics [1–3]. The phonon glass electron crystal model has guided efforts to reduce lattice thermal conductivity towards the amorphous limit [4–6] while maintaining electrical conductivity. Among various factors to be optimized, carrier-phonon coupling is one of the key considerations since it dictates both carrier and phonon transport. For example, previous studies show that lattice thermal conductivity can be dramatically reduced by carrier-phonon scattering when the carrier concentration in the semiconductor is considerable [7–9]. Particularly, coupling between carriers and acoustic phonons is both ubiquitous and essential because acoustic phonons are easily thermally populated and are leading heat carriers due to large group velocities. Acoustic deformation potential (ADP) is a standard to quantify carrier-acoustic phonon coupling, manifested as perturbation to electronic energy by strain from long-wavelength longitudinal acoustic (LA) phonons [10,11]. However, quantitative experimental characterization of ADP is challenging

largely due to difficulty in distinguishing various energy carrier scattering channels. It is even harder for thermoelectric materials, which often involve doping, defects, and multiple optical phonon branches. For example, electrically measured carrier mobilities correlate with the band-edge ADP parameters [10], but the presence of defects complicates the analysis by incurring impurity scattering.

Herein, we demonstrate ADP characterization for thermoelectric materials based on ultrafast spectroscopy of coherent acoustic phonon (CAP) dynamics. Mg_3Sb_2 , an attractive thermoelectric material due to ideal performance [12–15] and intriguing transport properties [16,17], is selected as the modeling system because carrier-acoustic phonon scattering is a key concern in its development [18–20] and its nearly isotropic structure [21] facilitates the phonon dynamics analysis. Through the relation between the amplitude of the CAP-induced oscillatory transient signal and the excitation photon energy, we show that the ADP mechanism and the thermoelastic (TE) effect [22,23] contribute comparably to CAP generation. By this relation, the ADP coupling constant ($\partial E_g/\partial \eta$, the derivative of the band gap versus the strain, a key ADP parameter) of Mg_3Sb_2 is extracted experimentally, consistent with the first-principles calculation result. This method relies on the transient Coulombic interaction between carriers and acoustic phonons and thus averts disturbance of other scattering channels. Most importantly, it is found that this method is particularly feasible for thermoelectric material

*These authors contributed equally to this work.

†Corresponding author: jiongy@t.shu.edu.cn

‡Corresponding author: liuws@sustech.edu.cn

§Corresponding author: guol3@sustech.edu.cn

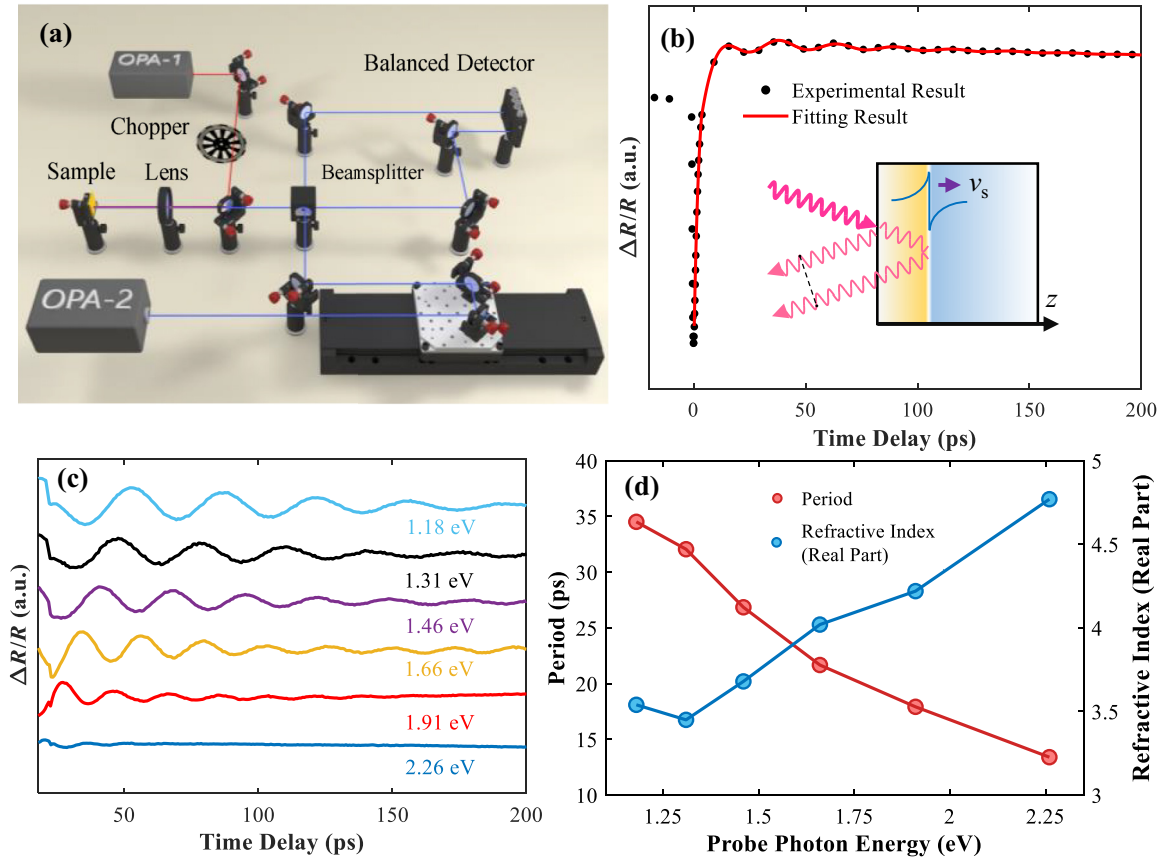


FIG. 1. (a) The schematic of the ultrafast spectroscopy system. (b) The transient reflectance signal with pump photon energy 3.1 eV and probe photon energy 1.55 eV. The pump fluence was 0.3 mJ/cm^2 . The inset illustrates the origin of the oscillatory signal. (c) The extracted oscillatory components of the transient reflectance signals for different probe photon energies with the same pump conditions as those in (b). (d) The oscillation period and the real part of the refractive index of Mg_3Sb_2 versus the probe photon energy.

study, because strong phonon anharmonicity and small band gaps make the measurement insensitive to the uncertainty of carrier diffusion coefficients, leading to additional improvement of accuracy. This work may facilitate further study in thermoelectrics along with fields such as superconductivity and polaron physics.

II. EXPERIMENTAL DETAILS

Ultrafast spectroscopy was performed on a polycrystalline Mg_3Sb_2 sample with a pump-probe system including a femtosecond laser and two optical parametric amplifiers (OPAs) for spectral tuning, as shown in Fig. 1(a). The output of an Yb:KGW femtosecond laser (Pharos-10 W, Light Conversion) at 1030 nm, 25 kHz was split by a beam splitter into two beams, the pump and the probe. The probe went through an OPA (Orpheus-F, Light Conversion) and has a <200 fs pulse duration. The pump went through another OPA (Orpheus-N-2H, Light Conversion) and a barium borate crystal, with a <180 fs pulse duration. The wavelengths of the two beams were independently tuned by the OPAs. The pump, modulated by a mechanical chopper at 500 Hz, was focused by a lens with 12.5 cm focal length and incident at an angle of 2.75° . The probe was delayed versus the pump by

a mechanical stage. The spot diameters of the focused pump and probe beams were 140–180 and <60 μm , respectively. The reflectance change at different moments after the pump excitation was measured by moving the stage. The signal was sent into a lock-in amplifier, which picked up the signal at 500 Hz for noise suppression. The synthesis method for the samples is shown in the Supplemental Material [24].

A typical transient reflectance signal is shown in Fig. 1(b). The signal consists of an initially abrupt and subsequently gradual change of reflectance and a long-lasting damped oscillatory part. The nonoscillatory part is related to photoexcited carrier dynamics, including interband transitions and carrier-phonon scattering. The oscillatory signal is attributed to excitation and propagation of a strain pulse, a wave packet of longitudinal CAPs. The CAPs escape from the sample surface at the sound velocity v_s and alter the dielectric constant in the sample, creating a moving interface. The probe is partially reflected from the surface while the transmitted part is partially reflected by the moving interface (Brillouin scattering), as shown in the inset of Fig. 1(b). The oscillatory response arises from the varying distance between the two interfaces with time, which causes an evolving phase lag between the two reflected beams and thus alternatively constructive and destructive interference.

To acquire the CAP-induced oscillatory signal, we used Eq. (1) to fit the transient reflectance signal and remove the carrier signal:

$$\Delta R/R = A_{e1}e^{-t/\tau_{e1}} + A_{e2}e^{-t/\tau_{e2}} + A_{osc}e^{-t/\tau_{osc}} \cos(2\pi t/T_p + \varphi), \quad (1)$$

where A_{e1} , A_{e2} are the carrier signal amplitudes, τ_{e1} , τ_{e2} are the characteristic times of the multiple-stage carrier relaxation, and t is the time delay between the pump and the probe. A_{osc} , τ_{osc} , T_p , and φ indicate the amplitude, damping time, Brillouin period, and initial phase of the oscillation. A representative fitting curve is shown in Fig. 1(b). Due to the interference nature, T_p should follow [28]

$$T_p = \frac{hc}{2E_{probe}n_R v_s}, \quad (2)$$

where n_R is the real part of the refractive index, h is the Planck constant, c is the light speed in vacuum, and E_{probe} is the probe photon energy. Figure 1(c) illustrates that T_p decreases as E_{probe} increases, which obeys Eq. (2) and justifies the origin of the oscillation signal. T_p and n_R for different E_{probe} are plotted in Fig. 1(d), extracted with the measured sound velocity 4187 m/s (see the Supplemental Material [24]). The grain dimensions in the sample are several microns while the probe spot diameter is tens of microns (see the Supplemental Material [24]). Therefore, the CAPs were launched along multiple crystalline orientations. Since the sound velocity of Mg_3Sb_2 is almost isotropic [29], a single value was applied here. The contribution from transverse acoustic phonons is neglected here since the oscillation signal has a pure frequency component [30,31].

III. THEORETICAL MODELING

Since Mg_3Sb_2 is centrosymmetric and opaque for the excitation photon energies, the inverse piezoelectric effect and electrostriction do not contribute to CAP generation [22]. The primary optical excitation mechanisms of the CAPs are thus the ADP mechanism and the TE effect. The generated stress $\Delta\sigma$ includes the electronic and the thermal parts [28,32]:

$$\Delta\sigma(z, t) = \Delta\sigma_{ADP} + \Delta\sigma_{TE} = \frac{\partial E_g}{\partial \eta} \Delta N(z, t) - 3B\beta \Delta T(z, t), \quad (3)$$

where $\Delta\sigma_{ADP}$ and $\Delta\sigma_{TE}$ represent the contributions from the ADP mechanism and the TE effect, B is the bulk modulus, and β is the linear thermal expansion coefficient. $\Delta N(z, t)$ and $\Delta T(z, t)$ are the photoexcited carrier density and lattice temperature rise depending on the depth z and time t , which can be solved with the pump parameters and the material properties. The photoexcited carriers impulsively perturb the Coulombic force on the lattice, causing the electronic stress.

We first separately calculate the strain caused by the individual stress. The stress under a single generation mechanism is

$$\sigma_{ADP}(z, t) = \rho v_s^2 \eta + \frac{\partial E_g}{\partial \eta} \Delta N(z, t), \quad (4)$$

$$\sigma_{TE}(z, t) = \rho v_s^2 \eta - 3B\beta \Delta T(z, t). \quad (5)$$

With the temporary assumption of no carrier or heat diffusion,

$$\Delta N(z, t) = \theta(t)\alpha(1 - R_{pump}) \frac{F}{E_{pump}} e^{-\alpha z}, \quad (6)$$

$$\Delta T(z, t) = \theta(t)\alpha(1 - R_{pump}) \frac{F}{E_{pump}} e^{-\alpha z} \frac{E_{pump} - E_g}{C_v}, \quad (7)$$

where θ denotes the step function, and α , R_{pump} , E_{pump} , F , and C_v are the absorption coefficient, the reflectance, the photon energy, the fluence of the pump, and the volumetric heat capacity, respectively. The elasticity equation that governs the CAP propagation is

$$\rho \frac{\partial^2 u(z, t)}{\partial t^2} = \rho v_s^2 \frac{\partial^2 u(z, t)}{\partial z^2} + \frac{\partial \Delta\sigma(z, t)}{\partial z}, \quad (8)$$

where ρ is the density, and it yields the lattice displacement $u(z, t)$. The gradient of the optically induced stress acts as a source term. Then the elasticity equations related to the ADP mechanism and the TE effect are

$$\frac{\partial^2 u(z, t)}{\partial t^2} = v_s^2 \frac{\partial^2 u(z, t)}{\partial z^2} + v_s^2 \alpha \eta_{0,ADP} e^{-\alpha z}, \quad (9)$$

$$\frac{\partial^2 u(z, t)}{\partial t^2} = v_s^2 \frac{\partial^2 u(z, t)}{\partial z^2} + v_s^2 \alpha \eta_{0,TE} e^{-\alpha z}, \quad (10)$$

$$\eta_{0,ADP} = -\frac{\alpha(1 - R_{pump})F}{\rho v_s^2 E_{pump}} \frac{\partial E_g}{\partial \eta},$$

$$\eta_{0,TE} = \frac{B\alpha(1 - R_{pump})F}{\rho v_s^2 E_{pump}} 3\beta \frac{E_{pump} - E_g}{C_v}. \quad (11)$$

These equations were solved with the initial conditions $u(z, 0) = 0$, $\partial u(z, t)/\partial t|_{t=0} = 0$, and the free boundary condition. By linear superposition, the induced total strain $\eta(z, t) = \partial u(z, t)/\partial z$ is described by Eqs. (12a) and (12b):

$$\eta(z, t) = -\frac{\eta_0}{2} [e^{-\alpha(z+v_s t)} (e^{\alpha v_s t} - 1)^2 - \theta(v_s t - z) \times (e^{-\alpha(z-v_s t)} + e^{\alpha(z-v_s t)})], \quad (12a)$$

$$\eta_0 = \eta_{0,ADP} + \eta_{0,TE} = \frac{\alpha(1 - R_{pump})F}{\rho v_s^2 E_{pump}} \times \left(-\frac{\partial E_g}{\partial \eta} + 3B\beta \frac{E_{pump} - E_g}{C_v} \right). \quad (12b)$$

This strain modifies the dielectric constant ε and causes the reflectance change (the strain-related part) following Eq. (13) (Re means the real part).

$$\frac{\Delta R(t)}{R} = \text{Re} \left[\frac{4ik}{1 - n^2} \int_0^\infty \frac{\partial \varepsilon}{\partial \eta} \eta(z', t) e^{2inkz'} dz' \right]. \quad (13)$$

The amplitude of the oscillatory signal A_{osc} then follows Eq. (14).

$$A_{osc} \propto \left| \eta_0 \frac{8nk^2}{4n^2k^2 + \alpha^2} \right|. \quad (14)$$

Here k is the probe wave number in vacuum and n is the complex refractive index at the probe wavelength. The detailed derivation for detection of the strain pulse is provided in the Supplemental Material [24].

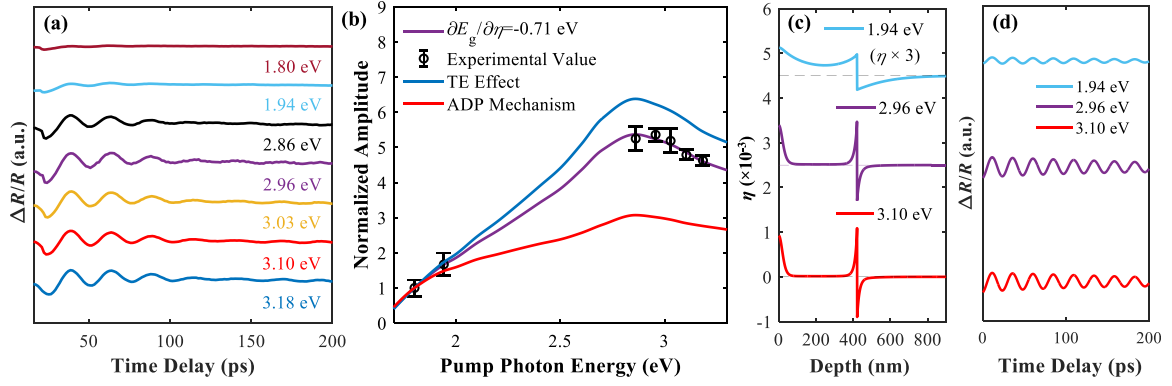


FIG. 2. (a) The oscillatory components of the transient reflectance signals for different E_{pump} (offset for clarity) when the probe photon energy was 1.55 eV and the pump fluence was 0.3 mJ/cm². (b) Theoretically predicted and measured $A_{\text{osc}}-E_{\text{pump}}$ relations normalized by the amplitudes at 1.8 eV. The red and blue lines represent the cases when the ADP mechanism and the TE effect dominates, respectively. The purple line represents the best fitting. The error bar corresponds to the standard deviation ($\times 3$) of three measurements. The calculated strain fields (c) and oscillatory transient reflectance signals (d) for $E_{\text{pump}} = 1.94, 2.96,$ and 3.10 eV.

IV. DISCUSSION

A. Characterization of the ADP coupling constant

This analytic expression with diffusion neglected facilitates the discussion on the role of E_{pump} and will be modified later. According to Eq. (14), when the probe parameters are fixed, A_{osc} is directly related to η_0 . The contributions have different expressions for the ADP mechanism $\eta_{0,\text{ADP}}$ and the TE effect $\eta_{0,\text{TE}}$ because the former is proportional to the excited carrier number density while the latter to the kinetic energy density within the carriers. With F fixed, $\eta_{0,\text{ADP}}$ scales with $1/E_{\text{pump}}$ while $\eta_{0,\text{TE}}$ scales with $(E_{\text{pump}} - E_g)/E_{\text{pump}}$. Therefore, the $A_{\text{osc}}-E_{\text{pump}}$ relations under the two mechanisms are distinguishable and can be used to evaluate the relative magnitude of the two contributions. Since the TE effect is described by the easily measurable thermal expansion coefficient, the ADP coupling constant can be determined by the measured $A_{\text{osc}}-E_{\text{pump}}$ relation. The CAP-induced oscillatory signals for different E_{pump} are shown in Fig. 2(a), which clearly shows the dependence of A_{osc} on E_{pump} .

The calculated $A_{\text{osc}}-E_{\text{pump}}$ relation can be used to fit the experimental results for obtaining the ADP coupling constant, provided that the diffusion effect is properly considered. The relevant physical properties of the Mg₃Sb₂ sample were experimentally measured, such as the carrier mobilities and thermal diffusion coefficient, while the absorption coefficient and the reflectance were obtained from first-principles calculations [33] (see the Supplemental Material [24]). The band gap was determined as 0.56 eV by the band structure calculations introduced later. With these properties, the influence of carrier and heat diffusion on the strain and the A_{osc} variation trend can be examined. As proposed previously [28], the dimensionless parameter $\xi_{a/t} = \alpha D_{a/t}/v_s$ quantifies the diffusion effect, where $D_{a/t}$ is the carrier or thermal diffusion coefficient. For large $D_{a/t}$, diffusion smears the carrier density or temperature gradient and reduces the driving force of the lattice displacement. With the measured electron and hole mobilities, $\mu_e = 149 \text{ cm}^2 \text{ V}^{-1} \text{ s}^{-1}$ and $\mu_h = 94 \text{ cm}^2 \text{ V}^{-1} \text{ s}^{-1}$, the corresponding carrier diffusion coefficients were $D_e = 3.85 \times 10^{-4} \text{ m}^2/\text{s}$ and $D_h = 2.43 \times 10^{-4} \text{ m}^2/\text{s}$ from the Einstein relation [34].

Then the ambipolar carrier diffusion coefficient was calculated as $D_a = 2D_e D_h / (D_e + D_h) = 2.98 \times 10^{-4} \text{ m}^2/\text{s}$ [35], corresponding to ξ_a values 0.332–6.734 for E_{pump} 1.8–3.18 eV. The ξ values on such orders indicate appreciable influence on the CAP dynamics, so carrier diffusion should be taken into account in calculating $\Delta N(z, t)$. Consistent with weak thermal conduction in Mg₃Sb₂, the thermal diffusion coefficient D_t is $9.97 \times 10^{-7} \text{ m}^2/\text{s}$, leading to tiny ξ_t values 0.001–0.023 for E_{pump} 1.8–3.18 eV, so the effect of heat diffusion is negligible.

The Green's function solutions of $\Delta N(z, t)$ and $\Delta T(z, t)$ including the effect of diffusion, Eqs. (15) and (16), were utilized for numerically solving $\eta(z, t)$ and the $A_{\text{osc}}-E_{\text{pump}}$ trend predicted by Eq. (14) was modified accordingly.

$$\Delta N(z, t) = \frac{\alpha(1 - R_{\text{pump}})F}{E_{\text{pump}}} \int_{-\infty}^{\infty} (4\pi D_a t)^{-1/2} \times \exp \left[-\frac{(z - z')^2}{4D_a t} - \alpha|z'| \right] dz', \quad (15)$$

$$\Delta T(z, t) = \frac{\alpha(1 - R_{\text{pump}})(E_{\text{pump}} - E_g)F}{E_{\text{pump}} C_v} \int_{-\infty}^{\infty} (4\pi D_t t)^{-1/2} \times \exp \left[-\frac{(z - z')^2}{4D_t t} - \alpha|z'| \right] dz'. \quad (16)$$

Figure 2(b) shows the calculated trends with diffusion when the ADP mechanism and the TE effect dominates, respectively. The two trends show well-distinguishable slopes, facilitating extraction of the ADP coupling constant. We used Eq. (1) to get the experimental values of A_{osc} , denoted by the black circles, and fitted the experimental data to determine $\partial E_g / \partial \eta$ as -0.71 eV, as shown by the purple line. With this ADP coupling constant, the strain fields at 100 ps were calculated for representative cases and plotted in Fig. 2(c). The corresponding oscillatory transient reflectance signals evaluated by Eq. (13) are shown in Fig. 2(d), well reproducing the experimental trend in Fig. 2(a).

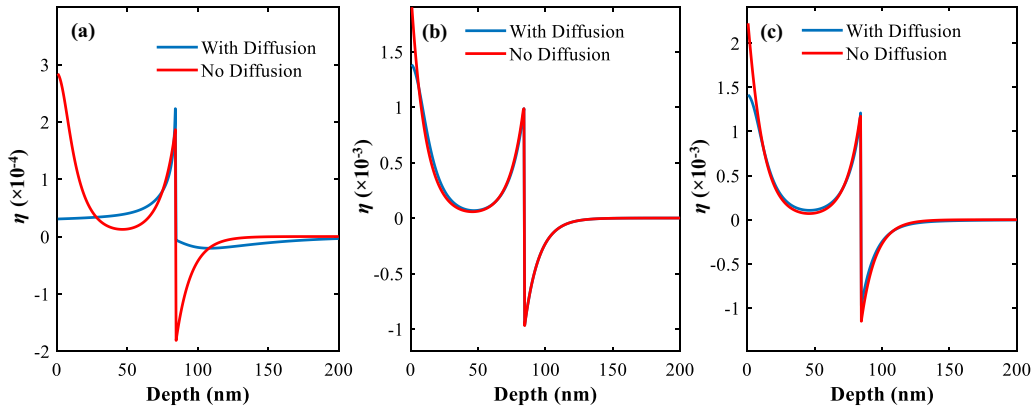


FIG. 3. The strain components generated by the ADP mechanism (a), by the TE effect (b), and the total strain by both the mechanisms (c) with or without diffusion considered. $E_{\text{pump}} = 3.18$ eV and $t = 20$ ps.

B. Effects of carrier and thermal diffusion

This CAP-based method for ADP characterization is effective when the ADP mechanism and the TE effect contribute comparably to CAP generation (the ratio of their contributions is $(\partial E_g / \partial \eta) C_v / [3B\beta(E_g - E_{\text{pump}})]$), in which case the variation trend of A_{osc} is sensitive to the change of the ADP coupling constant. Therefore, it may not be effective for semiconductors like Si and GaP for visible optical excitation, for which the ADP mechanism predominates [32]. For Mg_3Sb_2 , the anharmonic lattice vibration renders a high linear thermal expansion coefficient (about six times that of Si) [17] and the small band gap results in larger kinetic energy of carriers and more heat transferred to the lattice. These features make the TE effect substantial in Mg_3Sb_2 , benefiting the extraction of the ADP coupling constant. This strategy also applies to perovskites with highly anharmonic lattice vibration [36,37].

Interestingly, considering the diffusion effect (-0.71 eV) induces little change versus the result assuming no diffusion [-0.75 eV, fitted by Eq. (14)], in sharp contrast with materials like Ge [38]. This is related to the above-mentioned strong TE effect and poor heat conduction in Mg_3Sb_2 . At small E_{pump} , the absorption depth is large and the dimensionless parameters for both carrier and heat diffusion are small, making the diffusion effect negligible. At large E_{pump} , although carrier diffusion significantly changes the strain component due to the ADP mechanism as shown in Fig. 3(a), the leading strain component comes from the stronger TE effect, which is hardly affected by heat diffusion due to weak thermal conduction as shown in Fig. 3(b). Therefore, the carrier diffusion effect is not manifested in the CAP dynamics in Mg_3Sb_2 , as illustrated in Fig. 3(c). This benefits ADP characterization since carrier diffusion properties strongly depend on carrier and defect concentration and often incur large uncertainty.

High anharmonicity of lattice vibration causes strong phonon scattering and usually leads to low lattice thermal conductivity. Small band gaps generally ensure sufficient carriers at moderate temperature and thereby high electrical conductivity. These are common features of thermoelectric materials besides Mg_3Sb_2 . Therefore, the CAP-based method is fairly suitable for ADP characterization of thermoelectric materials due to the sensitivity in fitting and the weaker requirement on carrier diffusion quantification.

In order to examine the possible existence of Auger processes at high carrier density, the fluence dependence of the CAP-induced oscillatory signal was analyzed. As shown in Figs. 4(a) and 4(b), the amplitude of the CAP-induced oscillatory signal [extracted by Eq. (1)] is proportional to the pump fluence within the test range, consistent with Eq. (14). In our experiment, 0.3 mJ/cm^2 pump fluence was selected, which lies in the linear range. The linear relationship illustrates that the nonlinear effects, such as Auger processes, are not significant in the test range of our experiment. In addition, the temperature excursion by pump heating is below 70 K in this work, happening for the pump photon energy of 3.18 eV. Within this range, the heat capacity of Mg_3Sb_2 is not sensitive to temperature due to the low Debye temperature. The sound velocity and the density do not change significantly from 300 to 370 K [17], so the bulk modulus can be treated as a constant. In addition, the linear thermal expansion coefficient of Mg_3Sb_2 does not change significantly [17]. Therefore, within the temperature range, the involved physical properties are approximately constant and the temperature change does not affect our results. The transport properties such as the thermal diffusivity may change with temperature but the diffusion effect is not significant as discussed above. The detailed analysis is shown in the Supplemental Material [24].

V. FIRST-PRINCIPLES CALCULATIONS

First-principles calculations were used to evaluate $\partial E_g / \partial \eta$ for corroborating the experimental results. The band structure calculations were conducted based on density functional theory as implemented by the Vienna *Ab initio* Simulation Package with the plane-wave projector-augmented wave method. The generalized gradient approximation with the Perdew-Burke-Ernzerhof was utilized as the exchange-correlation functional. The atomic positions and the cell parameters of the Mg_3Sb_2 lattice were fully relaxed under each pressure. Brillouin-zone integrations were performed by using the k -point sampling of the Monkhorst-Pack scheme with an $11 \times 11 \times 7$ grid. The plane-wave energy cutoff was 450 eV and the convergence threshold was set as 10^{-6} eV in energy and 10^{-4} eV/Å in force. The modified Becke-Johnson potential was employed to obtain a more accurate band gap.

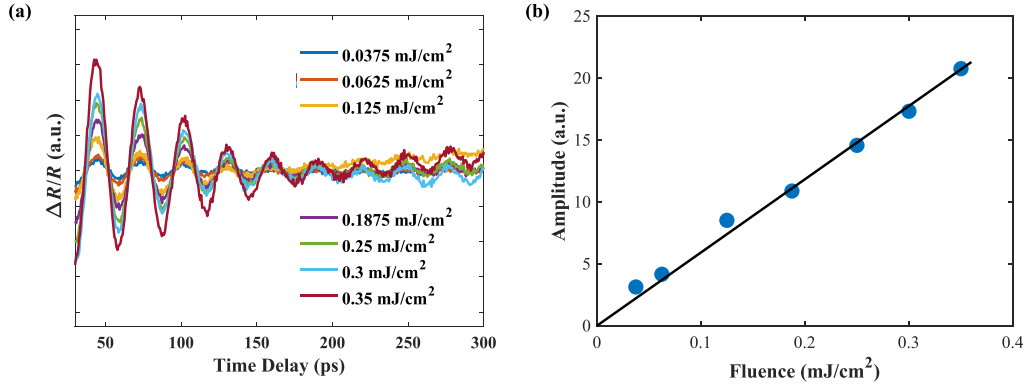


FIG. 4. (a) The extracted CAP-induced oscillatory components of the transient reflectance signals for different fluence with the same pump photon energy 3.1 eV. (b) The variation of the oscillation amplitude as a function of the pump fluence.

The band structure of Mg_3Sb_2 without pressurization is shown in Fig. 5(a). The valence band maximum resides at the Γ point while the conduction band minimum U^* lies in the Γ -M-L-A plane. The calculated band gap is 0.56 eV, comparable with the reported values [39,40]. To obtain the pressure-dependent electronic energy, the lattice was relaxed from 26 to 200 MPa, covering the experimental pressure range. The evolution of the conduction/valence band edge energies $E_{c/v}$ with pressure p are presented in Fig. 5(b) (left). The energy of the lowest-energy band was selected as the reference point, which hardly varies with pressure. The relationship between the band gap and pressure can be deduced as shown in Fig. 5(b) (right). From linear fitting, $\partial E_c/\partial p$ is 1.165×10^{-10} eV/Pa, $\partial E_v/\partial p$ is 1.005×10^{-10} eV/Pa, and $\partial E_g/\partial p$ equals 1.60×10^{-11} eV/Pa. Using the measured bulk modulus 48.5 GPa (see the Supplemental Material [24]), $\partial E_c/\partial \eta$, $\partial E_v/\partial \eta$, and $\partial E_g/\partial \eta$ are deduced to be -5.65 , -4.87 , and -0.78 eV, respectively, which are the key ADP parameters. The result agrees well with the experimental result (-0.71 eV).

The ADP theory has been shown to comply with first-principles calculations within the long-wavelength limit [7]. However, there lacks a perfect experimental method for ADP characterization. For example, carrier mobilities measured electrically are related to the square of the band-edge ADP parameters [$(\partial E_c/\partial \eta)^2$ and $(\partial E_v/\partial \eta)^2$] [10], but mobilities cannot tell the signs or exclude the effect of optical phonon scat-

tering. The CAP-based method relies on the transient carrier-acoustic phonon Coulombic interaction and can thus isolate this coupling channel, providing the ADP coupling constant $\partial E_g/\partial \eta$. These experimental and theoretical methods can cooperate to facilitate future study on carrier-phonon coupling.

Since the experimental and theoretical results in this work are consistent, the ADP information of Mg_3Sb_2 will be valuable for further study on this family of thermoelectric materials. Considering the competitive performance of n -type Mg_3Sb_2 , the electron-scattering rate is analyzed here for demonstration. The electron-scattering rate by LA phonons can be estimated from the ADP theory [41]:

$$\gamma_{e\text{-LA}} = \frac{(2\pi)^3 (\partial E_c/\partial \eta)^2 (2m_{ei})^{3/2} k_B T (E_e)^{1/2}}{h^4 \rho v_s^2}, \quad (17)$$

where m_{ei} is the inertial electron effective mass, k_B is the Boltzmann constant, and E_e is the electron kinetic energy. $\partial E_c/\partial \eta = -5.65$ eV was input with m_{ei} taken as the free-electron mass multiplied by 0.24 (see the Supplemental Material [24]). The prediction by Eq. (17) for 300 K is depicted in Fig. 6. First-principles calculations of the electron-scattering rates by different phonon modes were performed and those by LA phonons are plotted in Fig. 6 for comparison (see the Supplemental Material [24]). The agreement is reasonable between the results for electron energies below 0.25 eV, further justifying the obtained ADP information. For

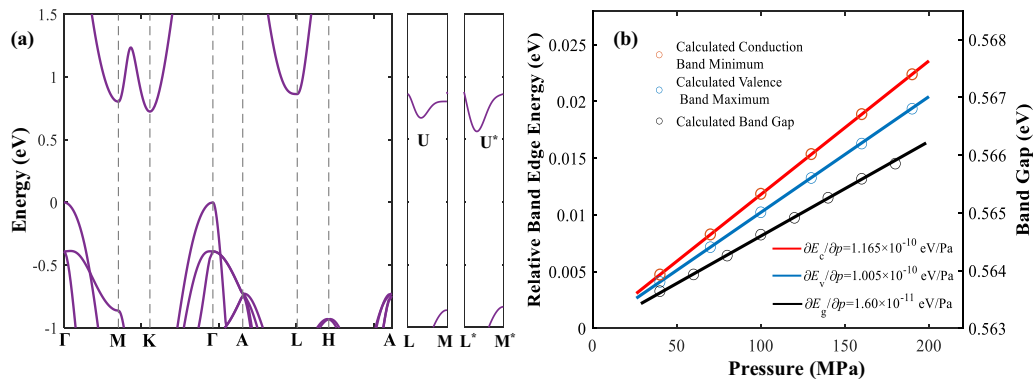


FIG. 5. (a) The band structure without pressurization. (b) The variation of the band-edge energies relative to those at zero pressure (left) and the band gap versus pressure (right). The circles and lines represent the calculated values and the fitting curves, respectively.

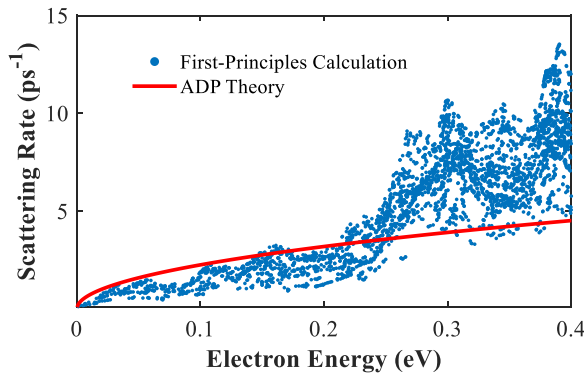


FIG. 6. The electron-scattering rates by LA phonons predicted by the ADP theory and first-principles calculations.

larger electron energies, the assumption of a fixed effective mass is improper, leading to failure of the ADP theory.

For Mg_3Sb_2 , there exist debates on carrier scattering mechanisms. Some experimental studies affirm the leading role of acoustic phonons above 300 K from the $T^{-1.5}$ dependence of the electrical properties [18–20], while first-principles calculations indicate the dominance of longitudinal optical phonon scattering [42], common for polar semiconductors [11,43]. This conflict may be resolved by future work comparing detailed information from experiments and theories. The ADP characterization is an important step for such mode-wise analysis of carrier-phonon scattering.

VI. CONCLUSIONS

In summary, we demonstrate ADP characterization for thermoelectric materials with ultrafast spectroscopy through CAP dynamics. With Mg_3Sb_2 as an example, the variation of the amplitude of the CAP-induced oscillatory signal versus the pump photon energy was used to experimentally quantify the ADP coupling constant, agreeing well with the theoretical results. The ADP information could facilitate performance optimization of and fundamental research on thermoelectric materials. Strong phonon anharmonicity and small band gaps, which are common features of thermoelectric materials, benefit ADP characterization by the CAP-based method and imply its wider applicability for studying transport physics.

ACKNOWLEDGMENTS

This work is partially supported by the National Science Foundation of China (52176075 and 52172216), Characteristic Innovation Project of the Department of Education of Guangdong Province (2022KTSCX109), the Introduced Innovative R&D Team of Guangdong (2017ZT07C062), and National Key R&D Program of China (2018YFB0703602). J.Y. acknowledges the support by Key Research Project of Zhejiang Laboratory (2021PE0AC02). S.S. acknowledges the support from Singapore Ministry of Education Academic Research Fund Tier 1 (A-0009121-00-00).

- [1] K. Pal, S. Anand, and U. V. Waghmare, *J. Mater. Chem. C* **3**, 12130 (2015).
- [2] A. Sakai, S. Minami, T. Koretsune, T. Chen, T. Higo, Y. Wang, T. Nomoto, M. Hirayama, S. Miwa, D. N. Hamane, F. Ishii, R. Arita, and S. Nakatsuji, *Nature (London)* **581**, 53 (2020).
- [3] L. Xie, J. H. Feng, R. Li, and J. Q. He, *Phys. Rev. Lett.* **125**, 245901 (2020).
- [4] G. A. Slack, *CRC Handbook of Thermoelectrics* (CRC Press, Boca Raton, 1995), pp. 400–432.
- [5] J. He and T. M. Tritt, *Science* **357**, eaak9997 (2017).
- [6] D. G. Cahill, S. K. Watson, and R. O. Pohl, *Phys. Rev. B* **46**, 6131 (1992).
- [7] B. Liao, B. Qiu, J. Zhou, S. Huberman, K. Esfarjani, and G. Chen, *Phys. Rev. Lett.* **114**, 115901 (2015).
- [8] B. Liao, A. A. Maznev, K. A. Nelson, and G. Chen, *Nat. Commun.* **7**, 13174 (2016).
- [9] J. Zhou, H. D. Shin, K. Chen, B. Song, R. A. Duncan, Q. Xu, A. A. Maznev, K. A. Nelson, and G. Chen, *Nat. Commun.* **11**, 6040 (2020).
- [10] J. Bardeen and W. Shockley, *Phys. Rev.* **80**, 72 (1950).
- [11] T.-H. Liu, J. Zhou, B. Liao, D. J. Singh, and G. Chen, *Phys. Rev. B* **95**, 075206 (2017).
- [12] H. Tamaki, H. K. Sato, and T. Kanno, *Adv. Mater.* **28**, 10182 (2016).
- [13] J. Zhang, L. Song, S. H. Pedersen, H. Yin, L. T. Hung, and B. B. Iversen, *Nat. Commun.* **8**, 13901 (2017).
- [14] J. Li, S. Zhang, F. Jia, S. Zheng, X. Shi, D. Jiang, S. Wang, G. Lu, L. Wu, and Z. Chen, *Mater. Today Phys.* **15**, 100269 (2020).
- [15] A. Li, C. Fu, X. Zhao, and T. Zhu, *Research* **2020**, 1934848 (2020).
- [16] W. Peng, G. Petretto, G. Rignanese, G. Hautier, and A. Zevalkink, *Joule* **2**, 1879 (2018).
- [17] Y. Zhu, Y. Xia, Y. Wang, Y. Sheng, J. Yang, C. Fu, A. Li, T. Zhu, J. Luo, C. Wolverton, G. J. Snyder, J. Liu, and W. Zhang, *Research* **2020**, 4589786 (2020).
- [18] J. Zhang, L. Song, A. Mamakhel, M. R. V. Jørgensen, and B. B. Iversen, *Chem. Mater.* **29**, 5371 (2017).
- [19] J. Shuai, J. Mao, S. Song, Q. Zhu, J. Sun, Y. Wang, R. He, J. Zhou, G. Chen, D. J. Singh, and Z. Ren, *Energy Environ. Sci.* **10**, 799 (2017).
- [20] K. Imasato, C. Fu, Y. Pan, M. Wood, J. J. Kuo, C. Felser, and G. J. Snyder, *Adv. Mater.* **32**, 1908218 (2020).
- [21] J. Zhang, L. Song, M. Sist, K. Tolborg, and B. B. Iversen, *Nat. Commun.* **9**, 4716 (2018).
- [22] P. Ruello and V. Gusev, *Ultrasonics* **56**, 21 (2015).
- [23] O. Matsuda, M. C. Larciprete, R. L. Voti, and O. B. Wright, *Ultrasonics* **56**, 3 (2015).
- [24] See the Supplemental Material at <http://link.aps.org/supplemental/10.1103/PhysRevB.108.064310> for details regarding sample synthesis, the relevant physical properties of Mg_3Sb_2 , detection of the strain pulse, the effect of temperature excursion, the details of first-principles calculations for optical properties and electron-scattering rates, the effective masses of carriers of Mg_3Sb_2 , and the scattering rates of electrons by different phonon modes in Mg_3Sb_2 , which includes Refs. [25–27].

- [25] M. T. Agne, K. Imasato, S. Anand, K. Lee, S. K. Bux, A. Zevalkink, A. J. E. Rettie, D. Y. Chung, M. G. Kanatzidis, and G. J. Snyder, *Mater. Today Phys.* **6**, 83 (2018).
- [26] S. Song, J. Mao, J. Shuai, H. Zhu, Z. Ren, U. Saparamadu, Z. Tang, B. Wang, and Z. Ren, *Appl. Phys. Lett.* **112**, 092103 (2018).
- [27] A. Li, C. Hu, B. He, M. Yao, C. Fu, Y. Wang, X. Zhao, C. Felser, and T. Zhu, *Nat. Commun.* **12**, 5408 (2021).
- [28] C. Thomsen, H. T. Grahn, H. J. Maris, and J. Tauc, *Phys. Rev. B.* **34**, 4129 (1986).
- [29] M. Jin, S. Lin, W. Li, X. Zhang, and Y. Pei, *Mater. Today Phys.* **21**, 100508 (2021).
- [30] O. Matsuda, O. B. Wright, D. H. Hurley, V. E. Gusev, and K. Shimizu, *Phys. Rev. Lett.* **93**, 095501 (2004).
- [31] M. Lejman, G. Vaudel, I. C. Infante, P. Gemeiner, V. E. Gusev, B. Dkhil, and P. Ruello, *Nat. Commun.* **5**, 4301 (2014).
- [32] K. Ishioka, A. Rustagi, U. Höfer, H. Petek, and C. J. Stanton, *Phys. Rev. B* **95**, 035205 (2017).
- [33] D. J. Singh and D. Parker, *J. Appl. Phys.* **114**, 143703 (2013).
- [34] C. Hu, *Modern Semiconductor Devices for Integrated Circuits* (Pearson/Prentice-Hall, Englewood, NJ, 2010), pp. 35–58.
- [35] O. B. Wright, B. Perrin, O. Matsuda, and V. E. Gusev, *Phys. Rev. B* **64**, 081202(R) (2001).
- [36] P. Mante, C. C. Stoumpos, M. G. Kanatzidis, and A. Yartsev, *Nat. Commun.* **8**, 14398 (2017).
- [37] B. Wu, W. Ning, Q. Xu, M. Manjappa, M. Feng, S. Ye, J. Fu, S. Lie, T. Yin, and T. C. Sum, *Sci. Adv.* **7**, eabd3160 (2021).
- [38] L. Li, F. He, X. Zhao, Z. Tong, and L. Guo, *Phys. Rev. B* **106**, L060304 (2022).
- [39] Y. Pan, M. Yao, X. Hong, Y. Zhu, F. Fan, K. Imasato, Y. He, C. Hess, J. Fink, J. Yang, B. Büchner, C. Fu, G. J. Snyder, and C. Felser, *Energy Environ. Sci.* **13**, 1717 (2020).
- [40] X. Shi, X. Zhang, A. Ganose, J. Park, C. Sun, Z. Chen, S. Lin, W. Li, A. Jain, and Y. Pei, *Mater. Today Phys.* **18**, 100362 (2021).
- [41] K. Koumoto and T. Mori, *Thermoelectric Nanomaterials, Materials Design and Applications* (Springer, New York, 2013).
- [42] F. Meng, S. Sun, J. Ma, C. Chronister, J. He, and W. Li, *Mater. Today Phys.* **13**, 100217 (2020).
- [43] T.-H. Liu, B. Song, L. Meroueh, Z. Ding, Q. Song, J. Zhou, M. Li, and G. Chen, *Phys. Rev. B* **98**, 081203(R) (2018).